The Influence of SO2 on the Corrosion of Mg and Mg-Al Alloys

Journal of The Electrochemical Society

The Influence of SO_2 on the Corrosion of Mg and Mg-Al Alloys

The Influence of SO_2 on the Corrosion of Mg and Mg-Al Alloys

M. Esmaily,[a,*,z] D. B. Blücher,[b] R. W. Lindström,[c,] J.-E. Svensson,[a,**] and L. G. Johansson[a]**

[a]*Department of Chemical and Biological Engineering, Chalmers University of Technology, SE-412 96 Gothenburg, Sweden*
[b]*SINTEF Materials and Chemistry, N-7465 Trondheim, Norway*
[c]*Department of Chemical Engineering and Technology, Applied Electrochemistry, KTH Royal Institute of Technology, SE-10044 Stockholm, Sweden*

The SO_2-induced atmospheric corrosion of some magnesium-aluminum (Mg-Al) alloys, including Mg alloy AZ91D, and commercially pure Mg (CP Mg) was investigated using well-controlled laboratory exposures and included real-time measurements of SO_2 deposition. The influence of SO_2 concentration, alloy composition, humidity, and ppb level additions of O_3 or NO_2 on the rate of SO_2 deposition was investigated. SO_2 accelerates the corrosion of Mg and Mg alloys causing localized corrosion, $MgSO_36H_2O$ being the dominant corrosion product. At 60% RH, traces of O_3 or NO_2 strongly increased both the SO_2 deposition and the corrosion rate. The rate of SO_2 deposition was strongly dependent on humidity; at 70% RH and higher the SO_2 deposition rate was very rapid and constant in time while it was transient below 50% RH. At 60% RH, a change from transient to rapid, steady-state, SO_2 deposition occurred. The sudden activation is explained by the onset of electrochemical corrosion. The activation behavior was shown to depend on SO_2 concentration, the thickness of the surface film and by the presence of ambient O_2.
 [DOI: 10.1149/2.0801506jes] All rights reserved.

Manuscript submitted February 11, 2015; revised manuscript received March 4, 2015. Published March 12, 2015.

Magnesium-aluminum (Mg-Al) alloys are widely used as structural materials in many engineering sectors as a result of their good castability and good mechanical properties at room temperature. Due to their low weight/strength ratio, these types of Mg alloys have found widespread applications; from portable microelectronics to automobiles and aircraft. However, Mg alloys are sensitive towards corrosion and exhibit the lowest corrosion potentials among the engineering metals.[1–4] Also, Mg and Mg-Al alloys exhibit high corrosion rates when immersed in NaCl (aq) solution, corrosion being more severe compared to other engineering alloys, including carbon steel. Nevertheless, Mg alloys exhibit somewhat better corrosion properties than steels under atmospheric conditions.[5–8] The causes behind the relatively slow corrosion of Mg-Al alloys in the atmosphere are still not fully clear.

Because Mg-Al alloys are often used in atmospheric conditions, a better understanding of the atmospheric corrosion properties is of importance. A large number of parameters affect the atmospheric corrosion process of Mg-Al alloys. Therefore, systematic studies are required to clarify their role on the corrosion. There have been extensive researches on the atmospheric corrosion behavior of Mg alloys using field studies that correlate corrosion rate to selected environmental parameters.[9–19] The variability and complexity of the outdoor atmosphere constitute a major problem when trying to correlate the corrosion rate of a metal to the concentration of, e.g., a particular trace gas in the environment. Laboratory studies under controlled conditions provide the opportunity to study the effect of a specific parameter and/or the synergic effects of atmospheric variable on the corrosion of metallic materials. For example, laboratory investigations have shown that carbon dioxide (CO_2) slows down the corrosion of Al, Zinc (Zn), Mg and Mg-Al alloys in the presence of NaCl.[8,20,21] Very recently, Esmaily et al.,[7] investigated the influence of exposure temperature on the atmospheric corrosion behavior of commercially pure Mg (CP Mg) and alloy AM50 using laboratory experiments and reported a strong positive temperature dependency of Mg-Al alloy AM50. The same exposures, however, revealed an unclear temperature dependency of CP Mg. The influence of microstructure on the atmospheric corrosion of Mg-Al alloys has also been widely studied.[22–31]

Table I lists the typical ambient concentrations of sulfur dioxide (SO_2), nitrogen dioxide (NO_2) and ozone (O_3).[32,33] O_3 and NO_2 are among the most important trace oxidants in the outdoor atmosphere, which often occur at higher concentration than SO_2, see for e.g. Table I. Field-based experiments have shown in several cases that trace levels of both gases can accelerate atmospheric corrosion in the presence of SO_2.[12,15] Since two decades ago, the atmospheric concentration of these corrosive gases has been increased significantly due to human activities, and thus their role on the corrosion behavior of various metals has become a challenge for corrosion scientists.[34,35] Both field investigations and lab studies have shown that acidic trace gases, especially SO_2, accelerate the atmospheric corrosion of many engineering alloys.[15–18,36–38] This is also the case for Mg and Mg alloys. Thus, significant amounts of sulfate-containing corrosion products are typically found on Mg and Mg alloys after exposure in both indoor and outdoor environments.[12,15,19] This is coming from the fact that CP Mg and Mg-Al alloys such as AM50 and AZ91D are excellent getters for SO_2 at 95% RH, the rate of SO_2 deposition being constant in time and independent of the presence of sodium chloride (NaCl).[12]

Hence, in this study we investigate the influence of SO_2 on the atmospheric corrosion of Mg and some Mg-Al alloys, such as AZ91D, using carefully controlled laboratory exposures. The influence of SO_2 on the mass gain of was studied and deposition of SO_2 was investigated thoroughly, including the effects of adding O_3 and NO_2. Further, the combined effects of SO_2 and NaCl were investigated. To our knowledge, this is the first laboratory study that deals with the effect of these gases on the corrosion of Mg-Al alloys. This study was motivated by interests in advancing the understanding of the effect of SO_2 and to some extent O_3 and NO_2, as important atmospheric variables, on the corrosion behavior of Mg-Al alloy in real atmospheric environments.

Experimental

Sample preparation.— This study includes a number of high-pressure die cast Mg-Al alloys as well as CP Mg from ingot with chemical compositions shown in Table II. The alloys were received from Husqvarna AB and Finnveden Metal Structures AB, Sweden. As-received materials were cut to produce 15 × 15 × 3 mm^3 corrosion coupons. The CP Mg ingot tested was 99.97% pure and bought from Johnson Matthey Puratronic. Prior to exposures, samples were ground on SiC paper (4000 mesh) in de-ionized water. Thereafter, the samples were polished with 1 μm diamond spray, whereas the Mg samples were polished with alumina slurry. Samples were then ultrasonically cleaned in acetone, dried in air and stored over a desiccant for 2 hours (h) before exposure. To investigate the deposition rate of SO_2 on MgO, single crystals with a dimension of 10 × 10 × 1 mm^3

*Electrochemical Society Student Member.
**Electrochemical Society Active Member.
zE-mail: mohsen.esmaily@chalmers.se

Table I. Typical peak concentrations of SO_2, NO_2 and O_3 in the troposphere over the continents.[32,33]

Pollutant	Remote	Rural	Moderately polluted	Heavily polluted
SO_2	1	1–30	30–200	200–500
NO_2	1	1–20	20–200	200–500
O_3	50	20–80	100–200	200–500

*Concentrations of the pollutants are given in part per billion (ppb).

that were supplied by the commercial thin film manufacturer SPI were used.

Gravimetric analysis.— After the exposures, the mass gain of the samples was registered after storing for one week over a desiccant at ambient pressure and temperature and this is termed the dry mass gain. The amount of corrosion products was determined by leaching and pickling the samples at ambient temperature using ultrasonic agitation. The water-soluble corrosion products and unreacted NaCl were removed by leaching in pure water (pH 7) in two steps, for 30 and 60 seconds. Thereafter, the samples were pickled up to five times in 20% CrO_3 (aq) at room temperature. The individual corrosion removal process lasted 15 or 30 seconds. To avoid the accumulation of anions in the pickling solution, the chromic acid was renewed before each pickling. The samples were then stored in a desiccator for one week prior to the weighing for determining the metal loss values. Self-corrosion during Cr-treatment was negligible. After pickling, the samples were rinsed with water and acetone.

Experimental setup.— All exposures in this study were performed in a well-controlled synthetic environment. The two main experimental approaches are displayed in Fig. 1. The four-week exposure (672 hour (h)) (Fig. 1a) was chosen to determine the mass gain and the formation of corrosion products, while Time-Resolved trace gas Analysis of the Deposition (TRAD) (Fig. 1b) was employed to investigate the deposition rate of SO_2, NO_2 and O_3 on Mg and Mg-Al alloys during the first 20 h of exposure. Both the exposure systems are made entirely of glass and Teflon. The samples were suspended by a thin nylon string in the middle of the chamber. The corrosion chambers were immersed in a water tank held at constant temperature (22.0 ± 0.3°C). To avoid condensation in the parts of the system outside the water tank the temperature in the room was kept at 25°C. The exposure gas was prepared from dried and purified air. Because the air purification system removes most of the CO_2 in the air we achieved a CO_2 concentration of 350 ppm (close to the atmospheric concentration of CO_2) by adding pure CO_2 from a cylinder and monitoring the concentration. Relative humidity (RH) was regulated to be 50–100% with an accuracy of ±0.5% by mixing dry air and air saturated with water vapor. SO_2 (g) and NO_2 (g) were added to the dry air stream using permeation tubes designed and manufactured by the authors. The permeation rates of the SO_2 tubes correspond to SO_2 concentrations of 48, 96 and 501 ppb in the exposure gas. The permeation rate of the NO_2 tube corresponded to a concentration of 200 ppb. The ozone was added to the dry purified air flow by means of an ozone generator (UV radiation, $\lambda < 230$ nm) to form atomic oxygen which then reacts with dioxygen molecules to form O_3 (g). The exposure reactors contained eight parallel chambers in the, see Fig. 1a. The gas flow (1 dm^3/min) was passing through each chamber in turn for 15 seconds. The net gas flow was 7 mm/sec corresponding to a Reynolds number (R_e) of about 25 in an empty chamber. The SO_2 content in the gas leaving each chamber was determined by absorbing in 1% H_2O_2 (aq) solution and analyzing as sulfate using ion chromatography. In order to determine the amount of SO_2 deposited on samples, we compared this analysis to the results obtained using two empty corrosion chambers that were used as blanks. After the completion of the 672 h exposures the dry mass gain of samples was determined after storing over a desiccant at ambient pressure and temperature for one week.

The TRAD system (Fig. 1b) was used for deposition of SO_2, NO_2 and O_3. The gas flow resulted in a net gas velocity of 2.7 cm/s (laminar flow conditions, $R_e = 50$). The setup consisted of a single exposure chamber with continuous flow and real-time analysis of SO_2, NO_x and O_3 in the output gas. SO_2, NO_2 and O_3 were added to the dry, purified air stream as described above. SO_2 was analyzed by a fluorescence instrument (Environnment AF21M), the sensitivity was

Table II. Composition (wt. %) of the alloys investigated.

Material	% Mg	% Al	% Zn	% Mn	% Si	% Fe	% Cu	% Ni	% Pb
CP Mg	99.97	0.003	0.005	0.0023	0.003	0.0018	0.0003	0.0002	0.001
AM20	97.4	2.1	0.04	0.4	0.01	0.0017	0.0016	0.0005	<0.0001
AM50	94.7	5.0	0.01	0.25	0.01	0.0016	0.0010	0.0007	<0.0001
AM60	93.7	6.0	0.01	0.25	0.01	0.0016	0.0010	0.0007	<0.0001
AZ91	90.1	8.9	0.74	0.21	0.008	0.0022	0.0007	0.0004	<0.0001

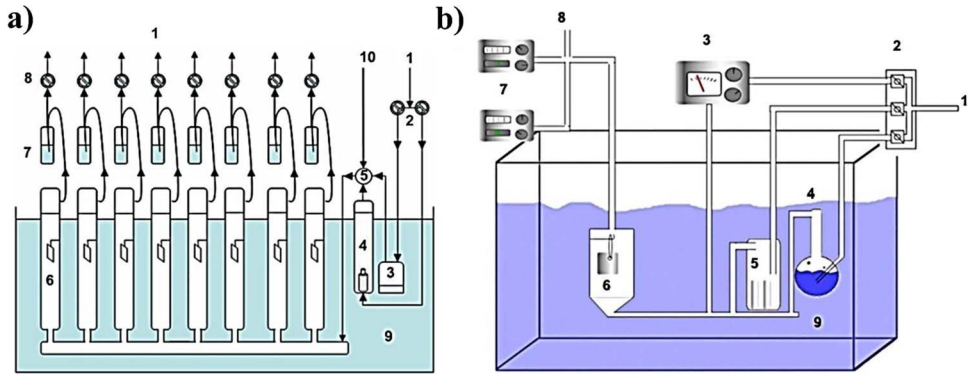

Fig. 1. (a) Experimental setup for exposures with some with ppb levels of SO_2 at 22°C. (1) pure air inlet; (2) mass flow regulators; (3) humidifier; (4) NO_2 and/or SO_2 permeation tubes; (5) mixing point; (6) exposure chambers; (7) gas trap; (8) solenoid valves; (9) thermostated water tank; (10) CO_2 or O_3 inlet; (11) carrier gas (purified air) for NO_2 and or SO_2. (b) The experimental setup of TRAD at 22°C. (1) pure air inlet with pure CO_2 (g) added from a cylinder; (2) mass flow regulators; (3) O_3 generator (UV light $\lambda < 230$ nm); (4) humidifier; (5) NO_2 and/or SO_2 permeation tubes; (6) exposure chambers with Al or Mg-Al samples; (7) real-time gas analyzers for SO_2, O_3 and NO_x-NO_2; (8) air outlet; (9) thermostated water tank.

1 ppb. The ozone concentration in the output gas was analyzed by using an instrument based on UV photometry (Dasibi 1108).

NO and NO_x were analyzed by a chemiluminescence instrument (Environnment AC 30M). Before the start of each experiment, the interaction of the pollutant with the reactor had reached a steady state so that the output gas from the corrosion chamber had a constant composition. The mass transfer-limited deposition of SO_2 was measured using an "ideal absorber", i.e. a glass plate ($30 \times 30 \times 3$ mm^3) with a thin layer of NaOH (aq). The deposition rate (ng/cm^2s) and the deposition velocity (cm/s) on the samples were determined by measuring the difference between the input and output concentrations of the pollutants. The deposition velocity V_d was defined as the flux of an air pollutant to a surface, divided by the concentration in the gas: $V_d = F/c$ where F is the flux to the surface (g/cm^2s) and c is the concentration of the pollutant in the gas (g/cm^3).[39,40] In our exposures, the concentration of the SO_2 was taken as the mean of the input and output concentrations in the cell. The same analytical techniques were used to analyze the samples after exposure as described above.

Ion Chromatography (IC) measurements.— Water-soluble corrosion products were removed by leaching in milli-q water (pH 7) for 1 minute and then for 30 minutes. The amount of water soluble anions removed by this process was determined by ion chromatography (Dionex DX100 with an Ionpac AD9-SC column). The flow rate was 2 ml/min and 1.8 mM Na_2CO_3 / 1.7 mM $NaHCO_3$ was used for elevations.

X-ray diffraction (XRD) analyses.— Grazing incidence X-ray diffraction (GI-XRD) was used for characterization of crystalline corrosion products (Siemens D-5000 CuKα radiation equipped with a Göbel mirror, Cu Kα radiation). The diffraction peaks of metallic Mg were used as an internal standard. The samples were also studied by ESEM (Electroscan 2020) and EDX (Link ISIS).

AFM/SKPFM.— Atomic Force Microscopy (AFM) with Scanning Kelvin Probe Force Microscopy (SKPFM) allowed us to study the initial stages of atmospheric corrosion. Previously, SKPFM was successfully used for investigating the corrosion on Al alloys, pure Al, duplex stainless steels, and on CP Mg.[41–44] A Nanoscope IIIa Multimode was used (Olympus micro cantilevers, n^+ silicon conductor, and a spring constant of about 27 N/m). In tapping mode, the topography and the Volta potential distribution were mapped simultaneously in situ with sub-micrometer resolution. The instrument was equipped with customized in situ cell to monitor the continuous corrosion process. The setup is described elsewhere.[45]

Fourier Transform Infrared Reflection Absorption Spectroscopy (FT-IRAS).— The in situ formation of corrosion products was monitored by Fourier Transform Infrared Reflection Absorption Spectroscopy (FT-IRAS) using a chamber with a volume of 27 cm^3, in which the sample was exposed laterally to the weathering gas. A Fourier transform infrared spectrometer (BIORAD FTS 60A) was connected to the exposure cell. The temperature of the gas was 22°C and the SO_2 concentration was about 200 ppm. IRAS spectra were recorded in absorbance units ($-\log R/R_0$), where R is the reflectance of the exposed sample and R_0 the background reflectance obtained after 0.5 h of exposure to a dry atmosphere. CP Mg and AZ91D were analyzed at high humidity (95% RH). The exposures lasted up to 2 h.

Analytical scanning electron microscope (SEM/EDX).— The morphology of the corrosion products was examined by an FEI Quanta 200 environmental scanning electron microscopy (ESEM) with a Schottky field emission gun (FEG). The instrument was equipped with Oxford Inca energy dispersive X-ray detector (EDX) system. Chemical composition analysis was performed with an Oxford Inca energy dispersive X-ray system (EDX). Imaging was performed using a range of acceleration voltages, 5 to 20 kV. SEM/EDX was used for local chemical analysis as well as elemental mapping of the corroded metal surfaces.

Results

Gravimetric results.— Table III lists the mass gains of CP Mg and AZ91D in different environments. The concentration of SO_2 was 48 ppb and the concentration of NO_2 and O_3 was 200 ppb. The samples were weighed every 168 hours but only the 672 h mass gains are shown. Both materials showed linear mass gains in the presence of SO_2. At 95% RH and 48 ppb SO_2, the accumulated mass gain of Mg after 672 h was 15 times higher than in the absence of SO_2. Table III also shows the fraction of the SO_2 in the corrosive atmosphere passing over the samples that was absorbed by the samples during the exposure. It may be noted that the fraction of SO_2 deposited on AZ91D at 95% RH was close to the maximum value attainable in the exposure system (as measured using a sample covered by a thin layer of NaOH (aq). This is in accordance with the short-term exposures described below; showing that SO_2 deposition on alloy AZ91D was in the transport-limited regime at 95% RH. The SO_2 deposition and mass gains were much lower at 60% RH. However, both the SO_2 deposition and mass gains at 60% RH increased significantly in the presence of NO_2 and O_3. Thus, after 4 weeks at 60% RH in the presence of $SO_2 + NO_2$ or $SO_2 + O_3$, mass gain was 4–5 times higher than when SO_2 was the only pollutant added. The effect of NO_2 and O_3 on SO_2 deposition is treated in greater detail below.

Corrosion product composition.— The only sulfur-containing corrosion product identified by XRD was Mg sulfite hexahydrate ($MgSO_36H_2O$). This corrosion product has also been reported for Mg-Al alloys exposed in an industrial outdoor environment.[15] The dominance of this compound in the corrosion product is supported by the mass gain and SO_2 deposition data in Table III, indicating that $MgSO_36H_2O$ accounted for most of the mass gain. The calculation was based on the assumption that all deposited SO_2 was present as

Table III. Mass gain and fraction of SO_2 deposited on CP Mg, and AZ91D after 672 hours.

Material	Environment	% RH	Fraction of SO_2 deposited (%)	Fraction of mass gain attributed to formation of $MgSO_3.6H_2O$	Dry mass gain (mg/cm^2)
Mg	Pure air	95	-	-	0.0055
AZ91	Pure air	95	-	-	0.005
Mg	SO_2	95	n.a.	n.a.	0.9
AZ91	SO_2	95	75	77	0.092
AZ91	SO_2	60	15	88	0.016
AZ91	$SO_2 + O_3$	60	60	88	0.065
AZ91	$SO_2 + NO_2$	60	65	62	0.076

The SO_2 concentration was 48 ppb, the NO_2 and O_3 concentrations were 200 ppb and temperature was 22°C. The mass gain results represent average values for triplicate samples. The scatter in mass gain was about ± 5%. The percentage of mass gain attributed to SO_2 deposition was calculated supposing that the deposited SO_2 forms $MgSO_3(H_2O)_6$ on the surface. The maximum fraction of SO_2 that can be deposited on the samples under the present experimental conditions corresponds to 75–80% of the SO_2 added to the exposure chambers.

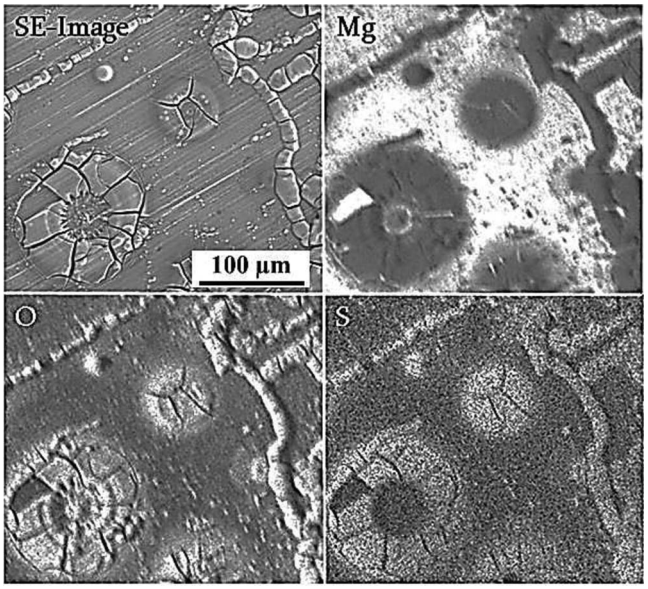

Fig. 2. SE-SEM image and EDX maps of Mg exposed to 49 ppb SO2 at 95% RH for 672 h. The temperature was 22°C. (a) Plane view SE-image; (b) Mg; (c) O; (d) S.

$MgSO_36H_2O$. The dominance of sulfite on the surface is in accordance with the in situ FTIR measurements described below. The remaining mass gain was attributed to hydroxides and carbonates. After exposure, the samples were leached in water and the leaching solutions were analyzed for anions using Ion Chromatography (IC). Both sulfite and sulfate were detected by IC analyses of samples exposed to SO_2. However, at least a part of the sulfate found by IC was formed during analysis, by oxidation of sulfite in aqueous solution. Supposing that the corrosion product formed on CP Mg in pure air at 95% was hydromagnesite ($Mg_5(CO_3)_4(OH)_24H_2O$) and that the corresponding product in air with 48 ppb SO_2 was $MgSO_36H_2O$, the loss of Mg after 672 h was calculated to be 1.7 µg/cm^2 in the former case and 12 µg/cm^2 in the latter case.

SEM and EDX analyses.— After 672 h exposure in the corrosive environment the Mg samples had lost their luster and were dark. Optical microscopy inspections revealed a transparent, glassy layer on the sample surface. The SEM images in Fig. 2 show more or less circular areas, about 100 µm in diameter, together with elongated shapes, both features corresponding to corrosion product accumulations on the surface. Working with pure Mg in aqueous sodium chloride (NaCl) solutions, Williams et al.[46] reported the formation of corrosion products with similar corrosion morphologies. The EDX analyses showed that the corrosion products were enriched in oxygen and sulfur. The center of the circular corrosion products contains oxygen but relatively little sulfur. Based on the XRD and gravimetric analyses above, it is concluded that the corrosion product agglomerations are dominated by $MgSO_36H_2O$. The observation that the circular areas are cracked is tentatively attributed to shrinking of the corrosion product by the loss of water from $MgSO_36H_2O$ during imaging. Figure 3 shows ESEM/EDX maps of a corroded AZ91 surface after exposure for 672 h in 49 ppb SO_2 at 95% RH. Similar to CP Mg, large corrosion product accumulations enriched in S and O were observed. Again, the relative sulfur content was lower at the center of the circular features. The β-phase, showing a network-like morphology, is clearly seen both in the secondary electron (SE) micrograph and in the Al map. The β-phase network was not visible on an unexposed sample, indicating that SO_2-induced corrosion affects the α- and β-phase differently, creating an etching effect. The Mg-rich α-phase regions exhibit higher oxygen yields compared to the β-phase (see O map in Fig. 3).

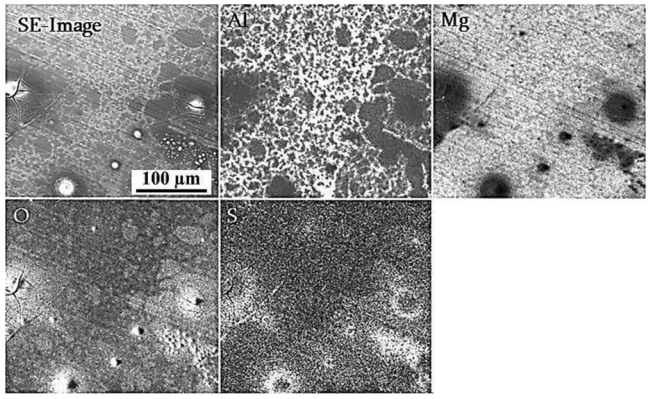

Fig. 3. SE-SEM and EDX maps of AZ91 exposed to 49 ppb SO_2 at 95% RH. (a) Plane view SE- image; (b) Al; (c) Mg; (d) O; (e) S.

In situ corrosion experiment using FTIR and SKPFM.— To study the initial formation of surface species in the presence of SO_2, time-resolved IR spectra were obtained from CP Mg and alloy AZ91D during exposure in the presence of 200 ppb SO_2 at different humidities. Figure 4 shows spectra measured at 95% RH in air. Absorption bands appear at 3000–3600, 1650, 900–1150 and at around 700 cm^{-1}, the bands growing with exposure time. The band at about 2350 cm^{-1} is an artefact due to CO_2(g). The broad band at 3000–3600 cm^{-1} is attributed to OH stretching vibrations in water and in surface hydroxide. The H_2O bending vibration is seen at around 1650 cm^{-1}. The surface water is attributed to adsorbed water and to solid salt hydrates. The lack of evidence for Mg sulfate on the surface in the SO_2 exposures (see below) implies that the surface water cannot be attributed to $MgSO_4$ (aq) solution (solid $MgSO_4$ is reported to form a solution at RH >86% at 22°C).[47] In the absence of SO_2, the two water bands did not grow appreciably during exposure. This indicates that in the presence of SO_2, much of the water on the surface belongs to solid compounds accumulating as a result of corrosion. The negative peak appearing at 3700 cm^{-1} upon exposure to SO_2 is characteristic of brucite ($Mg(OH)_2$). It is considered that brucite is present on the sample surface before exposure and is consumed by the reaction with SO_2. The region 850–1250 cm^{-1} corresponds to S-O stretching vibrations in sulfur-oxygen anions.[48] The broad peak centered around 980 cm^{-1} is attributed to surface sulfite. For $MgSO_3(H_2O)_6$(s), the corresponding peak appears at 936 cm^{-1}.[49] The presence of surface sulfite is in accordance with the identification of $MgSO_3(H_2O)_6$(s) by XRD after prolonged exposure to SO_2 in air (see below). The

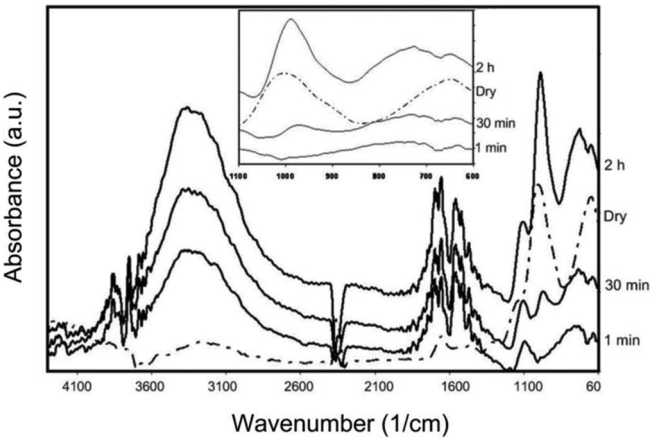

Fig. 4. Infrared absorption spectra at 200 ppb SO_2 on Mg at 95% RH. The dry spectrum was recorded after pure air had passed through the reaction chamber for 30 minutes.

accumulation of water on the surface in the presence of SO_2 is attributed to the formation of hydrated surface sulfite. No bands appeared that could be unambiguously attributed to sulfate. This is in contrast to the behavior of e.g., zinc.[50] The FT IRAS spectra obtained in N_2/SO_2 were essentially the same as in air/SO_2. The absorption bands formed upon exposure to SO_2 at 60 and 50% RH were qualitatively the same as at 90% RH but the bands were weaker and did not grow as rapidly. At high RH, the spectra obtained from AZ91D and CP Mg were qualitatively the same. At lower humidity, the growth of the sulfite bands was slower for AZ91D than for Mg. To summarize, the FT IRAS results show that SO_2 forms sulfite on Mg and on AZ91D and that there is little evidence for oxidation to sulfate.

Figure 5 shows in situ SKPFM time-resolved measurements on Mg at 60% RH in air with 49 ppb SO_2. The left column shows the surface topography, showing the formation and growth of discrete corrosion product accumulations on the surface. The features had a diameter of about 0.1 μm after one hour, and grew with time. After 5 h exposure they had partly coalesced and covered most of the surface. The right column shows the Volta potential maps. A comparison of the two columns shows that the growing features tended to exhibit a relatively low potential, indicating that these areas were anodic to the surrounding surface.

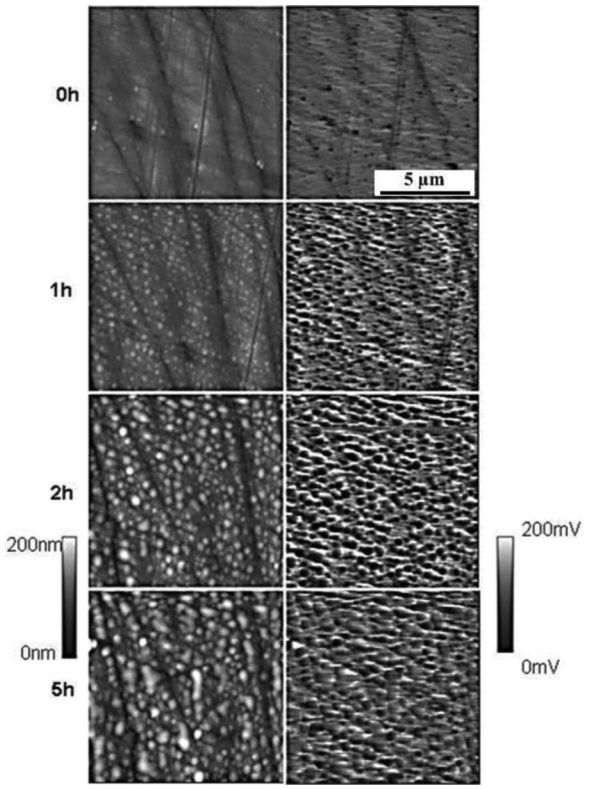

Fig. 5. Time-resolved in situ AFM and SKPFM images of Mg. The images in the left hand column show the topography by tapping mode AFM while the right hand column shows Volta potential maps imaged by SKPFM. The brighter areas are protruding from the surface in the topography images and have a higher relative potential in the Volta potential images. The top row shows the Mg surface at the start of the experiment and the lower rows show the surface after 1, 2 and 5 hours. Note: The height range is 200 nm and the Volta potential range is 200 mV. (RH: 60%, T: 22°C, SO2 (g): 49 ppb).

SO_2 deposition.— The rate of SO_2 deposition on the samples was investigated during the first 20 h of exposure. The influence of relative humidity, SO_2 concentration, alloy composition and pretreatment as well as the effect of O_2 and traces of O_3 and NO_2 were investigated. Figure 6a shows the deposition of SO_2 on Mg and on alloy AZ91D at different humidity as a function of exposure time. The SO_2 concentration was 49 ppb. At high humidity (>70% RH), SO_2 deposition was very rapid and constant with time on both materials. The SO_2 deposition rate was equal to that measured for an identical sample that had been covered by a thin layer of NaOH (aq). This value represents the maximum SO_2 deposition rate that can be attained in the exposure set-up, given the flow conditions, sample size and temperature. It represents the gas-transport limited value for deposition, meaning that all SO_2 molecules that impinged on the surface were deposited. At 60% RH, SO_2 deposition was initially in the gas-transport limited regime but rapidly slowed down, signifying a saturation of the surface. AZ91D showed such saturation at higher RHs than CP Mg, as seen in Fig. 6a. At 50% RH, SO_2 deposition on AZ91D and CP Mg dropped to 1–2% of the maximum value after 12 h.

The SO_2 concentration dependence.— In order to compare SO_2 deposition at different SO_2 concentrations it is useful to introduce the concept deposition velocity V_{dep}, (see Fig. 6b). The deposition velocity is equal to the deposition rate of SO_2 on the sample surface (g/m^2s) divided by the concentration of SO_2 in the gas (g/m^3). Thus, the unit of the quotient is ms^{-1}. The SO_2 concentration was taken as the average of the input and output concentrations in the reaction chamber. At high humidity, SO_2 deposition was in the transport-limited regime throughout the SO_2 concentration range studied (49–501 ppb), corresponding to a deposition velocity of 0.26 cm/s in the experimental conditions, deposition rate being proportional to SO_2 concentration. At lower humidity the situation was different, as illustrated in Fig. 6b, showing SO_2 deposition velocity on CP Mg and AZ91D as a function of exposure time at 60% RH for three different SO_2 concentrations. Initially, the deposition velocity equaled the transport-limited value of 0.26 cm/s in all cases. With time, V_{dep} decreased, corresponding

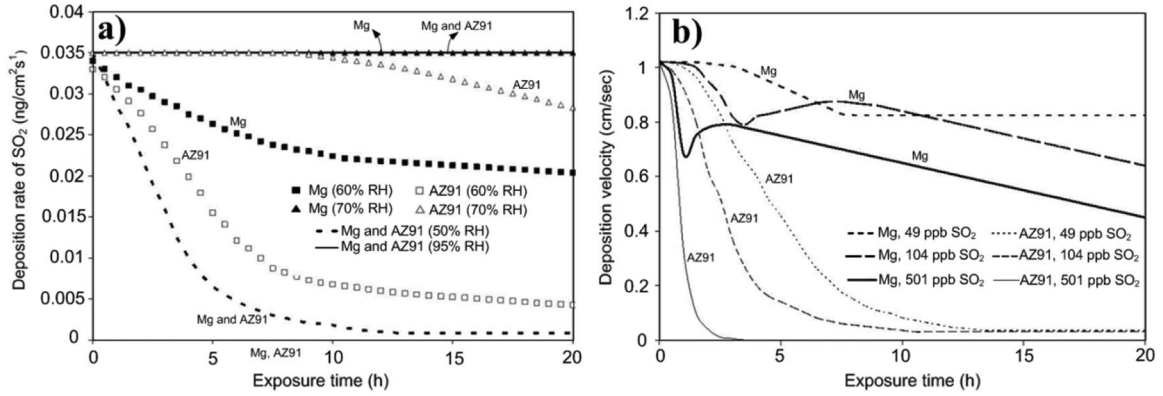

Fig. 6. Deposition of SO_2 on Mg and on alloy AZ91; (a) SO_2 deposition as a function of exposure time in air with 49 ppb SO_2 at different RHs, (b) influence of SO_2 concentration on the SO_2 deposition velocity at 60% RH.

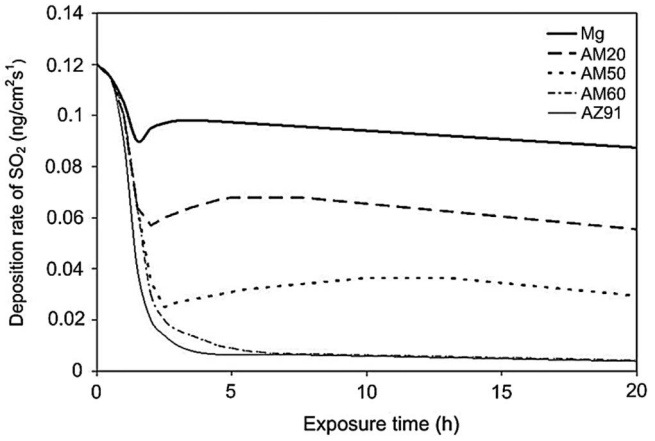

Fig. 7. SO_2 deposition rate as a function of Al content in the Mg-Al alloys at 60% RH. The SO_2 concentration was 264 ppb.

to a saturation of the surface with respect to SO_2. As expected, V_{dep} dropped off more rapidly at higher SO_2 concentration. It may be noted that the SO_2 deposition velocity slowed down much more rapidly for AZ91D than for CP Mg. The two materials differed also in another respect. Thus, while V_{dep} dropped monotonically with time for AZ91D, there was a change in curvature in the case of CP Mg. Thus, after the initial decrease, the deposition velocity increased again on CP Mg, corresponding to an activation of the surface. The change of curvature (activation behavior) was especially evident at the highest SO_2 concentration (501 ppb).

The influence of alloy composition.— The observation that the SO_2 deposition behavior of CP Mg was different from that of AZ91D motivated an investigation of the dependence of the SO_2 deposition rate on Al content. Fig. 7 illustrates the rate SO_2 deposition of several Mg-Al alloys exposed to 264 ppb SO_2 at 60% RH. Initially, deposition was in the transport limited regime and therefore independent of alloy composition. After 20 h exposure, the deposition rates showed a strong dependence on Al content, the two alloys with more than 6% Al exhibiting very low deposition rates. The activation behavior was more pronounced on the alloys low in Al. Exposure to at 60% RH for 20 h resulted in limited corrosion and it was not possible to reliably determine the mass loss. In contrast, mass losses after 672 h exposure at 95% RH were measurable. In that case, there was a strong dependence of corrosion rate on alloy composition. Thus, the registered mass loss values were ~0.042, 0.068, 0.072, 0.11 and 0.34 mg/cm^2 for alloy AZ91D, AM60, AM50, AM20 and CP Mg, respectively.

The effect of pre-exposure on SO_2 deposition.— The change in curvature of the SO_2 deposition curves for CP Mg at medium humidity has already been noted (see Figs. 6a and 6b). To test whether this behavior was caused by surface de-passivation and initiation of corrosion, we studied the effect of pre-exposure in clean humid air. Thus, Mg was first exposed for 13 h in clean air at 95% RH in order to form a surface film that was considerably thicker than the air-formed film present after polishing. The Mg sample was then exposed to SO_2 at 60% RH. The resulting SO_2 deposition in Fig. 8a, indicated that the pre-exposed sample exhibited a much stronger decrease in SO_2 deposition rate with time than the reference sample. Notably, the pre-exposed sample showed no upturn in the SO_2 deposition curve. This supports the interpretation of the upturn of the SO_2 deposition curve as evidence for a corrosion process that starts after surface de-passivation.

SO_2 deposition on single crystal MgO.— Because the experiments with pre-exposed samples imply that deposition of SO_2 on Mg involves both reaction with the surface film and corrosion of the underlying metal, it was decided to investigate SO_2 deposition on MgO. Thus, the deposition of SO_2 on a single crystal MgO specimen (10 × 10 × 1 mm^3) was measured at different RHs at a SO_2 concentration of 49 ppb (not shown). At 95% RH, the behavior of MgO towards SO_2 was similar to that of CP Mg, SO_2 deposition being in the transport-limited regime. In contrast, the SO_2 deposition velocity on MgO at 60% RH was small and soon dropped below the limit of detection. This was the case in air as well as in N_2. As noted above, CP Mg and alloy AZ91D exhibited relatively rapid SO_2 deposition at this humidity, especially in air.

The effect of O_2/N_2 on SO_2 deposition.— Figure 8b shows the effect of replacing O_2 by N_2 on SO_2 deposition on CP Mg at 60% RH. To our surprise, the rate of deposition of SO_2 in N_2 was only about one third of that measured in air. Also, all SO_2 deposition curves acquired in air and in pure oxygen at 60% RH featured an activation step whereas the exposure in N_2 did not. It may be noted that the N_2 environment included traces of O_2 (on the order of 100 ppm). The presence of oxygen had a similar but smaller effect on the rate of deposition of SO_2 on alloy AZ91D. In the case of single crystal MgO, the SO_2 deposition curves in air and in N_2 were the same.

The influence of NO_2 and O_3 on the deposition rate of SO_2.— Figure 9 shows the influence of 200 ppb NO_2 in air on the SO_2 deposition rate for AZ91D. The SO_2 concentration was 48 ppb and RH was 50, 60 and 70%. At 50% RH, the introduction of NO_2 only increased the SO_2 deposition initially and the effect prevailed for less than an hour. At 60% RH, the introduction of NO_2 strongly increased SO_2 deposition so that it became mass-transfer limited. The increased deposition rate prevailed for as long as NO_2 was added. At 70% RH, SO_2 deposition was already in the transport limited regime in the absence of NO_2 (compare Fig. 2). Hence the rate of SO_2 deposition at 70% RH was not influenced by NO_2. The spikes in the curves when NO_2 was added are due to instability in the gas flow. The effect of ozone on SO_2 deposition was similar to that of NO_2 (Fig. 10). However, the effect of ozone extended to lower humidity (compare

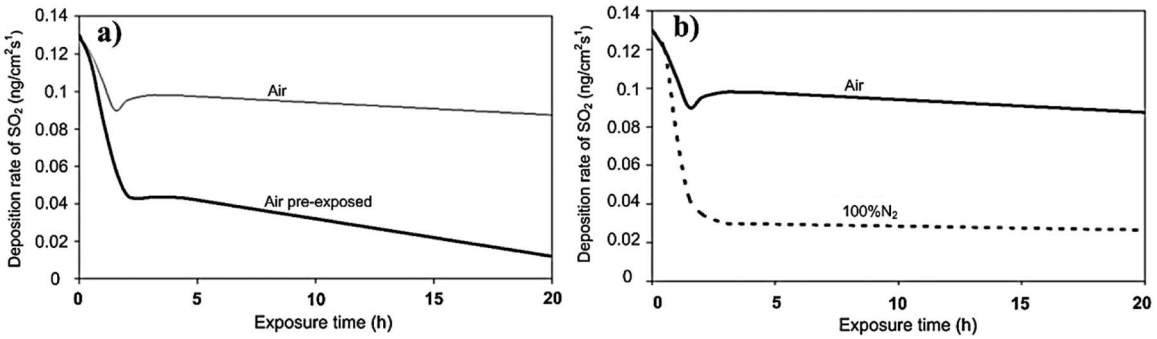

Fig. 8. (a) Influence of pre-exposure on the deposition of SO_2 on Mg. RH was 60% and the SO_2 concentration was 264 ppb, (b) influence of O_2 on the deposition of SO_2 on Mg. RH was 60% and the SO_2 concentration was 264 ppb.

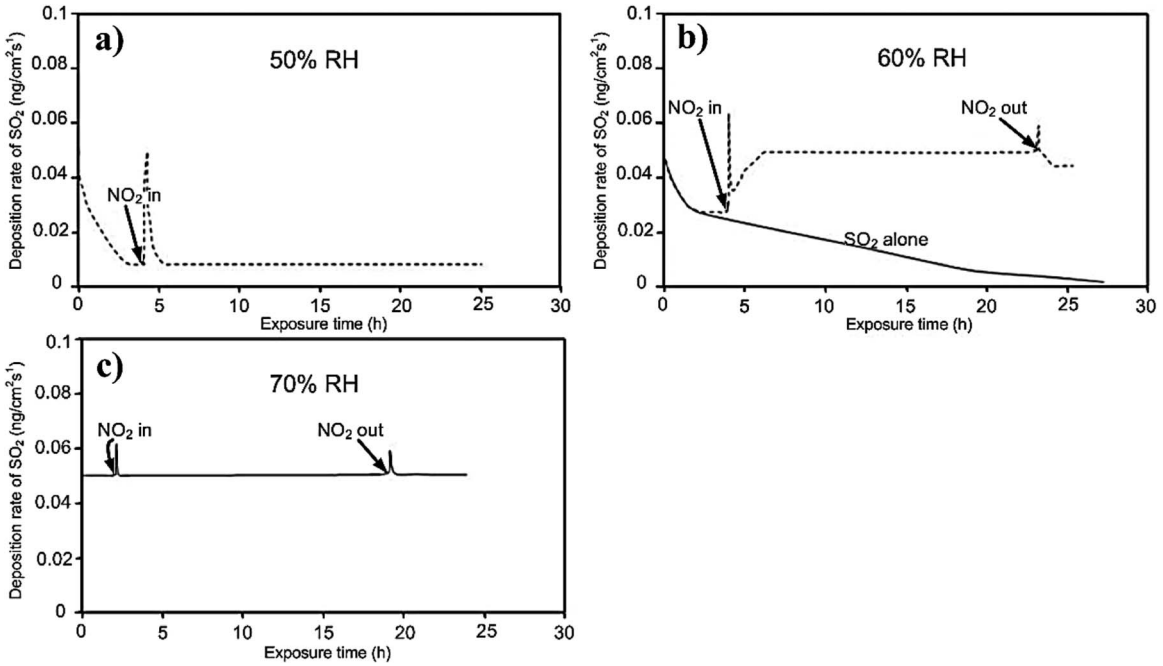

Fig. 9. Influence of addition of 200 ppb NO_2 on SO_2 deposition on polished AZ91 samples at 50, 60 and 70% RH. The SO_2 concentration was 48 ppb.

the 50% RH curves in Figs. 9 and 10). At 40% RH and below, the introduction of O_3 only resulted in a slight and temporary increase of the SO_2 deposition rate.

Desorption of SO_2.— Finally, the desorption of SO_2 was investigated by transferring CP Mg and AZ91D samples, that had been exposed to SO_2-containing (264 ppb) in air with different humidity for 2 h, to a reactor with flowing clean humid air and analyzing the output gas for SO_2 (not shown). The results showed that samples exposed to SO_2 at 95% RH did not desorb measurable amounts of SO_2 (<1ppb) while samples exposed to SO_2 at 60% RH and lower exhibited small but measurable SO_2 desorption when exposed to clean air at both 60 and 95% RH. This shows that SO_2 which is adsorbed at 60%RH is more loosely bonded to the surface than SO_2 which is adsorbed at 95% RH.

Discussion

The gravimetric data and the SO_2 deposition studies (Table III and Fig. 6a) show that the surface of Mg and AZ91D are almost ideal absorbers for SO_2 at 95% RH and 49 ppb SO_2. In contrast to e.g., zinc (Zn),[39] copper (Cu)[51] and Al[52] the oxidation of (IV)-valent sulfur on the Mg and Mg-Al alloy surface appears to be slow. Thus, the only corrosion product detected by XRD after 672 h at 95% RH and

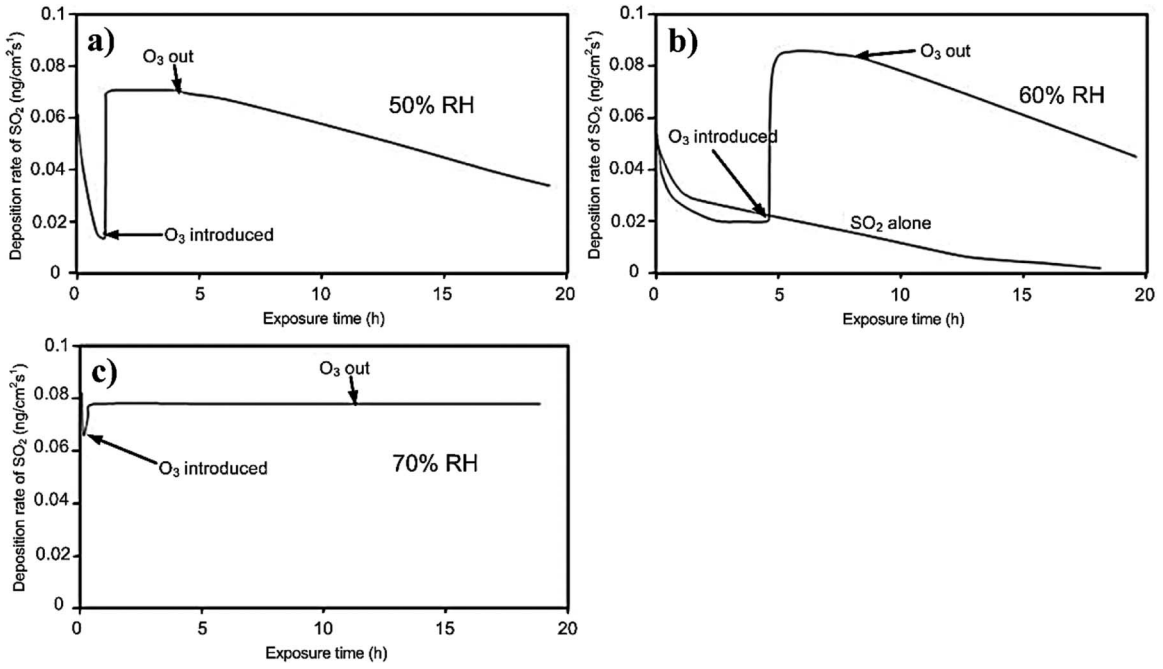

Fig. 10. Influence of addition of 200 ppb O_3 on SO_2 deposition on polished AZ91 samples at 50, 60 and 70% RHs. The SO_2 concentration was 48 ppb.

49 ppb SO_2 was Mg sulfite, $MgSO_3 6H_2O$, and in situ FTIR investigation provided no evidence for sulfate formation. The dominance of $MgSO_3 6H_2O$ in the corrosion product (Table III) implies that SO_2 only speeds up corrosion to the extent that, in principle, all Mg ions generated in corrosion form sulfite. Hence, it could be argued that corrosion in air at high RH in the presence of SO_2 is chemical rather than electrochemical in nature. In such a scenario the protective oxide/hydroxide surface film reacts with SO_2 and dissolves in an aqueous surface film. The resulting thinning of the protective film then results in the formation of new oxide by a Cabrera Mott type mechanism. In this way, the rate of oxidation is determined by the rate of film thinning which, in turn is determined by the rate of SO_2 deposition. The ability of MgO to react rapidly with SO_2 at high humidity in the absence of a metal substrate is indeed verified by the observation that single crystal MgO is an ideal getter for SO_2 at 95% RH.

However, the present results do not support a purely chemical corrosion mechanism. Thus, the tiny corrosion product aggregates formed initially and visualized by SKPFM (Fig. 5), indicate that corrosion in the presence of SO_2 is localized from the beginning, implying a separation of anodic and cathodic areas. Indeed, the observation of large circular corrosion product accumulations on both Mg and alloy AZ91D after 672 h (SEM images in Figs. 3 and 4) indicate that electrochemical cells have been active on the surface. This is also true for the etching effect observed on alloy AZ91D (Fig. 3). Below, the present observations concerning the kinetics of SO_2 deposition on the samples are discussed in the context of the corrosion of the metal.

Before going into the details of the effect of SO_2 on Mg corrosion it is appropriate to mention the corrosion properties of Mg in humid air, in the absence of SO_2. In dry air Mg is oxidized by O_2, forming a surface oxide (passive film) by a Cabrera-Mott type mechanism. In the presence of water vapor the film becomes partly hydroxylated forming a $MgO/Mg(OH)_2$ layer.[1,53,54] Also, CO_2 in ambient air reacts with the film to form a very thin surface layer.[6] It has been reported that the amount of water adsorbed on an oxide surface at 95% RH in ambient temperature air corresponds to an average of about 10 monolayers.[55] According to[56] the Cabrera-Mott passive film on Mg tends to dissolve in this liquid-like adsorbed water film. The authors claim that the resulting thinning of the passive film causes oxidation of Mg by O_2 to be resumed. As a result of dissolution of the relatively soluble passive film, the aqueous film becomes supersaturated, causing brucite to precipitate. After an induction period and running parallel to this process, an electrochemical corrosion process starts, involving anodic dissolution of Mg and hydrogen evolution, and giving rise to localized corrosion. In this scenario, the fast and sustained deposition of SO_2 measured at high RH is explained by the presence of a $Mg(OH)_2$ (aq)-containing aqueous film with high pH (equation 1). Because of the dissolution of SO_2, the aqueous surface film is acidified (equation 2), hence increasing its ability to dissolve new passive film. Also, the sulfite generated forms weak complexes with Mg^{2+},[48] further enhancing film dissolution. The dissolved Mg ions are expected to form adsorbed sulfite (equation 3) as well as forming the sparingly soluble Mg sulfite hexahydrate (equation 4) which was observed:

$$MgO + H_2O \leftrightarrows Mg^{2+}(aq) + 2OH^-(aq) \quad [1]$$

$$SO_2(g) + 2OH^-(aq) \rightarrow H_2O + SO_3{}^{2-}(aq) \quad [2]$$

$$SO_3{}^{2-}(aq) + Mg^{2+}(aq) \leftrightarrows MgSO_3(ads) \quad [3]$$

$$MgSO_3(ads) + 6H_2O(ads) \rightarrow MgSO_3.6H_2O(s) \quad [4]$$

In this way the process of Mg oxidation by O_2 in combination with SO_2 deposition becomes self-sustained. It is conceivable that under some circumstances Mg sulfite may passivate the surface. However, this was not observed. It may be noted that the lack of SO_2 desorption from samples exposed to SO_2 at high humidity (see results section) implies that a high pH prevails on the surface, indicating that the surface electrolyte is in contact with MgO or $Mg(OH)_2$.

At low RH the process just described is not operational because of the absence of a liquid-like water on the passive film surface that can dissolve the passive film. However, SO_2 is readily adsorbed on the film surface, forming sulfite according the following equation:

$$Mg(OH)_2(surface) + SO_2(g) \rightleftarrows MgSO_3(ads) + H_2O \quad [5]$$

The SO_2 deposition measurements at low humidity (<60% RH) (See Fig. 6a) show that the uptake of SO_2 is transient. Also, the desorption measurements revealed that SO_2 uptake is partially reversible. The transient deposition and the presence of loosely bonded S(IV) on the surface is in accordance with reaction 5, showing the tendency for the Mg surface to become saturated with SO_2.

At medium humidity (60% RH), the SO_2 deposition curve for Mg in air in some cases exhibits a characteristic upturn after a few hours (see, e.g. Figs. 6b and 7). It is argued that this signifies a transition from the low humidity behavior to the high humidity behavior. Thus, the change in curvature denotes the transition from a transient mode of SO_2 deposition, where part of the surface S(IV) is reversibly bound (reaction 5), to a steady-state mode of SO_2 deposition where SO_2 is irreversibly bound to the surface (reactions (1–4)). It is considered significant that this change of curvature was absent in N_2 environment and that it was also absent in the case of MgO in air. The observation that Mg metal and oxygen are both necessary for the change in curvature in the SO_2 deposition curve to occur implies that the transition is related to a reaction that involves both Mg metal and oxygen. Considering the role of O_2 in the atmospheric corrosion of Mg in humid air proposed by,[57] it is suggested that the activation of SO_2 deposition is caused by surface de-passivation and initiation of corrosion. Thus, the upturn of the SO_2 deposition curve is interpreted as the commencement of the process of passive film dissolution and Mg oxidation by O_2. In this way a slow but sustained corrosion process is started that generates fresh Mg hydroxide. In this scenario, the induction period of a few hours before the upturn of the SO_2 deposition curve corresponds to the time needed for the passive film to be sufficiently thinned for Mg oxidation by O_2 to start, the ability of the surface water film to dissolve the passive film being limited due to the relatively low RH. A similar upturn of the SO_2 deposition curve has been reported for zinc.[58] In that case the effect was reported to involve the oxidation of surface sulfite to sulfate. However, because of the lack of evidence for sulfate formation the change of curvature cannot be explained thus in the present case.

As was already mentioned, there is compelling evidence for electrochemical processes occurring on the corroding Mg surface. It is tentatively suggested that the large scale features seen after 672 h exposure (Figs. 3 and 4) are related to the electrochemical mode of corrosion suggested by,[58] involving hydrogen evolution and that the circular features result from the migration of sulfite ions towards anodic sites in the center.

The localized corrosion attack on AZ91D in air with 49 ppb SO_2 at 95% RH is illustrated in the SEM images in Fig. 3. The Mg rich α-phase is seen to be preferentially attacked. This is in accordance with previous SKPFM measurements at this laboratory that show that the α-phase is anodic to the intemetallic β-phase particles ($Mg_{17}Al_{12}$).[6,59]

At high RH (95%), the SO_2 deposition rate is equally fast on both CP Mg and AZ91D (see Fig. 6a). This is in accordance with the results from the four week exposures (see Table III). In contrast, at 60% RH the interaction between SO_2 and the metal depends strongly on alloy composition, the SO_2 deposition rate decreasing with increasing Al content (see Fig. 7). Also, the change of curvature in the SO_2 deposition rate on CP Mg at 60% RH discussed above, becomes less marked with increasing Al content and is absent in the high Al alloys (AM60 and AZ91D). The MgAl alloys included in this study have microstructures dominated by α-Mg and intermetallic β-phase particles ($Mg_{17}Al_{12}$), the volume fraction of a-Mg being >85%. Hence the surface properties of the alloys, such as SO_2 deposition, are expected to be dominated by α-Mg. It has been shown that the passive film on α-Mg in Mg-Al alloys is enriched in Al.[8,60] In comparison to Mg

oxide, alumina is much less soluble in neutral and acidic environment.[61] It is therefore expected that the dissolution of the passive film by the acid formed by the hydrolysis of SO_2 (see reactions 1–4 above) will be become increasingly slow as the Al content in the substrate increases. This is suggested to explain the differences observed between Mg and Mg-Al alloys regarding SO_2 deposition at 60% RH. Apparently, the protective properties of the alumina-containing film are not sufficient to protect the material at high RH. The observation that increasing Al content in the alloy results in a lower activity towards SO_2 is thus attributed to the corresponding increase in the Al content of α-Mg. It may be noted that for MgAl alloys, the Al content of the α-Mg phase also depends on alloy fabrication. Hence, it has been shown that the Al content in α-Mg in alloy AZ91D can be increased by modifying the casting technology, resulting in improved corrosion properties.[62]

The presence of ppb levels of ozone and NO_2 strongly increases the SO_2 deposition on AZ91D at 60% RH (see Figs. 9 and 10). The strong influence of O_3 and NO_2 at 60% RH can be seen also in the four-week exposures (see Table III), the mass gains in the combined $SO_2 + O_3$ and $SO_2 + NO_2$ environments being 4–5 times higher than for exposures with SO_2 alone. It is argued that this effect has the same origin as the effect of oxygen on SO_2 deposition on CP Mg (see above). Thus, it is argued that the molecules themselves or some reaction product on the surface act as oxidants on the surface of the passive film:

$$O_3 + H_2O + 2e^- \rightarrow O_2(g) + 2OH^- \qquad E^\circ = 1.24\ V \qquad [6]$$

$$2NO_2 + 2OH^- \rightarrow NO_2^- + NO_3^- + H_2O \qquad [7]$$

$$NO_2^- + H_2O + e^- \rightarrow NO(g) + 2OH^- \qquad E^\circ = -0.46\ V \qquad [8]$$

$$NO_3^- + H_2O + 2e^- \rightarrow NO_2^- + 2OH^- \qquad E^\circ = -0.01\ V \qquad [9]$$

The resulting increased formation of alkali would then explain the higher rate of SO_2 deposition in the presence of ozone and NO_2. It may be noted that, at 60% RH, the corrosion products were the same whether O_3 and NO_2 were present or not. In all cases, $MgSO_36H_2O$ (s) was the only crystalline corrosion product detected.

Conclusions

The SO_2-induced atmospheric corrosion of CP Mg and several Mg-Al alloys was investigated by means of laboratory exposures in humid atmospheres containing trace amounts of air pollutants namely ozone (O_3) and nitrogen dioxide (NO_2). The observations and findings are as follows;

- The presence of SO_2 in ppb levels accelerates the atmospheric corrosion of CP Mg and Mg-Al alloys. A linear mass gain was registered both at 95 and 60% RH in the presence of 49 ppb SO_2 during four weeks of exposure.
- The SO_2-induced corrosion of CP Mg and the investigated Mg-Al alloys is localized, indicating the presence of electrochemical cells. Magnesium sulfite ($MgSO_36H_2O$) was the dominant corrosion product formed.
- At low relative humidity SO_2 deposition on CP Mg is a transient process that terminates when the surface of the oxide film is covered by S(IV) species. At high humidity, the rate of SO_2 deposition on CP Mg and Mg alloy AZ91D is very high and limited by the mass transfer in the gas phase. At medium humidity, (60% RH) SO_2 deposition on CP Mg exhibits a characteristic change in curvature corresponding to the transition from a transient mode of SO_2 deposition to a rapid, steady-state mode of deposition where SO_2 is irreversibly bound to the surface.
- The observed activation behavior was inhibited by a thicker passive film, by higher Al alloy content, and by removal of ambient O_2, indicating that it was caused by the onset of electrochemical corrosion of Mg, part of the cathodic current being supplied by O_2 reduction.
- At 60% RH, the addition of O_3 or NO_2 strongly increased the SO_2 deposition rate on alloy AZ91D. This effect is explained by O_3 and NO_2 acting as cathodic depolarizers, providing cathodic current for the corrosion of CP Mg.

Acknowledgments

The authors are grateful to the Corrosion Department at KTH, Stockholm for letting us perform the IRAS measurements at their instrument. The authors would also like to express their thanks to The Swedish Foundation for Strategic Research (SSF) for funding this project.

References

1. G. L. Song and A. Atrens, *Adv. Eng. Mater.*, **5**, 837 (2003).
2. O. Lunder, J. E. Lein, T. K. Aune, and K. Nisancioglu, *Corrosion*, **45**, 741 (1989).
3. M. Grabowski, D. Bluecher, M. Korte, and S. Virtanen, *Corrosion*, **70**, 1008 (2014).
4. M. Esmaily, M. Shahabi-Navid, N. Mortazavi, J. E. Svensson, M. Halvarsson, M. Wessén, A. E. W. Jarfors, and L. G. Johansson, *Mater. Charac.*, **95**, 50 (2014).
5. J. R. Kish, Y. Hu, J. Li, W. Zheng, and J. R. McDermid, *Corrosion*, **68**, 468 (2012).
6. G. L. Song and A. Atrens, *Adv. Eng. Mater.*, **1**, 11 (1999).
7. M. Esmaily, M. Shahabi-Navid, J. E. Svensson, M. Halvarsson, L. Nyborg, Y. Cao, and L. G. Johansson, *Corros. Sci.*, **90**, 420 (2015).
8. M. Shahabi-Navid, M. Esmaily, J. E. Svensson, M. Halvarsson, L. Nyborg, Y. Cao, and L. G. Johansson, *J. Electrochem. Soc.*, **161**, C277 (2014).
9. Z. Cui, X. Li, K. Xiao, and C. Dong, *Corros. Sci.*, **76**, 243 (2013).
10. J. Liao, M. Hotta, S. Motoda, and T. Shinohara, *Corros. Sci.*, **71**, 53 (2013).
11. M. Jönsson, D. Persson, and C. Leygraf, *Corros. Sci.*, **50**, 1406 (2008).
12. L. Yang, Y. Li, Y. Wei, L. Hou, and Y. Tian, *Corros. Sci.*, **52**, 2188 (2010).
13. J. Chen, J. Q. Wang, E. H. Han, and W. Ke, *Corr. Eng., Sci. Tech.*, **46**, 277 (2011).
14. M. Zhaoa, P. Schmutz, S. Brunner, M. Liua, G. L. Song, and A. Atrens, *Corros. Sci.*, **51**, 1277 (2009).
15. Y. G. Li, Y. H. Wei, L. F. Hou, and P. J. Han, *Corros. Sci.*, **69**, 67 (2013).
16. L. Hao, S. Zhang, J. Dong, and W. Ke, *Corros. Sci.*, **59** 270 (2012).
17. Y. Ma, Y. Li, and F. Wang, *Corros. Sci.*, **51**, 997 (2009).
18. W. Chen, L. Hao, J. Dong, and W. Ke, *Corros. Sci.*, **83**, 155(2014).
19. Z. Cui, X. Li, K. Xiao, and C. Dong, *Corros. Sci.*, **76**, 243 (2013).
20. R. Lindström, On chemistry of atmospheric corrosion, Doctoral thesis, Department of Chemistry, Göteborg University, Göteborg, 2003.
21. D. Bluecher, R. Lindström, J. E. Svensson, and L. G. Johansson, *J. Electrochem. Soc.*, **148**, B127 (2001).
22. G. L. Song, *Adv. Eng. Mater.*, **7**, 563 (2005).
23. G. L. Song, A. Atrens, D. StJhon, J. Nairn, and Y. Li, *Corros. Sci.*, **39**, 855 (1997).
24. M. Jönsson, D. Persson, and R. Gubner, *J. Electrochem. Soc.*, **154**, C684 (2007).
25. O. Lunder, J. E. Lein, T. Kr Aune, and K. Nisancioglu, *Corrsion*, **45**, 741 (1989).
26. X. Y. Sun, B. Zhang, H. Q. Lin, Y. Zhou, L. Sun, J. Q. Wang, E.-H. Han, and W. Ke, *Corros. Sci.*, **77**, 103 (2013).
27. R. M. Asmussen, P. Jakupia, M. Danaie, G. A. Botton, and D. W. Shoesmith, *Corros. Sci.*, **75**, 114 (2013).
28. R. M. Asmussen, W. J. Binns, P. Jakupi, and D. W. Shoesmith, *J. Electrochem. Soc.*, **161**, C501 (2014).
29. M. Esmaily, N. Mortazavi, M. Shahabi-Navid, J. E. Svensson, M. Halvarsson, L. Nyborg, Y. Cao, M. Wessén, A. E. W. Jarfors, and L. G. Johansson, *J. Electrochem. Soc.*, **162**, C85 (2015).
30. M. Danaie, R. M. Asmussen, P. Jakupia, D. W. Shoesmith, and G. A. Botton, *Corros. Sci.*,**77**, 151 (2013).
31. M. Danaie, R. M. Asmussen, P. Jakupia, D. W. Shoesmith, and G. A. Botton, *Corros. Sci.*,**83**, 299 (2014).
32. B. J. Finlayson-Pitts and J. N. Pitts, *Atmospheric chemistry fundamentals and experimental techniques*, John Wiley and sons, New York (1986).
33. T. E. Graedel, *Corros. Sci.*, **27**, 721 (1987).
34. Z. Y. Chen, D. Liang, G. Ma, G. S. Frankel, H. C. Allen, and R. G. Kelly, *Corros. Eng. Sci. Technol.*, **45**, 169 (2010).
35. D. Liang, H. C. Allen, G. S. Frankel, Z. Y. Chen, R. G. Kelly, Y. Wu, and B. E. Wyslouzil, *J. Electrochem. Soc.*, **157**, C146 (2010).
36. S. Oesch and M. Faller, *Corros. Sci.*, **39**, 1505 (1997).
37. C. Kleber, R. Wiesinger, J. Schnöller, U. Hilfrich, H. Hutter, and M. Schreiner, *Corros. Sci.*, **50**, 1112 (2008).
38. W. S. Lassiter, *J. Phys. Chem.*, **76**, 1289 (1972).
39. J. E. Svensson and L. G. Johansson, *J. Electrochem. Soc.*, **140** 2210 (1993)
40. J. A. Garland, *Atmos. Environ.*, **12**, 249 (1978).
41. P. Schmutz and G. S. Frankel, *J. Electrochem. Soc.*, **145**, 2295 (1998).
42. M. F. Hurley, C. M. Efaw, P. H. Davis, J. R. Croteau, E. Graugnard, and N. Birbilis, *Corrosion*, In press (2014).
43. V. Guillaumin, P. Schmutz, and G. S. Frankel, *J. Electrochem. Soc.*, **148**, B163 (2011).
44. S. K. Kim, I. J. Park, D. Y. Lee, and J. G. Kim, *J. Appl. Electrochem.*, **43**, 507 (2013).

45. D. Blueher, J. E. Svensson, L. G. Johansson, M. Rohwerder, and M. Stratmann, *J. Electrochem. Soc.*, **151**, B621 (2014).
46. G. Williams, N. Birbilis, and N. McMurray, *Faraday Disscuss*., in press (2015).
47. Z. Ha and C. K. Chan, *J. Geoph. Res.*, **99**, 18801 (1994).
48. H. D. Lutz, S. M. El-Suradi, and B. Engelen, *Z. Naturforsch. B*, **32**, 1230 (1977).
49. L. Yang, Y. Wei, L. Hou, and D. Zhang, *Corros. Sci.*, **52**, 345 (2010).
50. J. E. Svensson and L.-G. Johansson, *Proceedings of the 12th International Corrosion Congress*, Houston, USA, (1993): p. 662.
51. H. Strandberg and L. G. Johanson, *J. Electrochem. Soc.*, **14**, 2334 (1997).
52. D. Bluecher, J. E. Svensson, and L. G. Johansson, *J. Electrochem. Soc.*, **152**, B397 (2005).
53. N. Thomas, N. V. Medhekar, G. S. Frankel, and N. Birbilis, *Curr. Opin. Solid State Mater.* Sci., In press (2014).
54. G. S. Frankel, A. Samaniego, and N. Birbilis, *Corros. Sci.*, **70**, 104 (2013).
55. P. B. P. Phipps and D. W. Rice, *ACS Symp. Ser.*, **89**, 235 (1979).
56. N. Cabrera and N. F. Mott, *Rep. Progr. Phys.*, **12**, 163 (1948).
57. R. Lindström, L. G. Johansson, G. E. Thompson, P. Skeldon, and J. E. Svensson, *Corros. Sci.*, **46**, 1141 (2004).
58. Q. Qu, C. Yan, Y. Wan, and C. Cao, *Corros. Sci.*, **44**, 2789 (2002).
59. M. Esmaily, M. Ström, J. E. Svensson, M. Halvarsson, and L. G. Johansson, *CORROSION*, in press (2015).
60. J. H. Nordlien, K. Nisancioglu, S. Ono, and N. Masuko, *J. Electrochem. Soc.*, **144**, 461 (1997).
61. M. J. N. Pourbaix, *Atlas of Electrochemical Equilibriums in Aqueous Solutions.* 2nd ed, (1974).
62. M. Esmaily, N. Mortazavi, J. E. Svensson, M. Halvarsson, D. B. Blücher, A. E. W. Jarfors, M. Wessén, and L. G. Johansson, submitted to *J. Electrochem. Soc.* (2015).